A Graph-Based Approach for Automatic Cardiac Tractography

Carole Frindel,* Marc Robini, Joël Schaerer, Pierre Croisille, and Yue-Min Zhu

A new automatic algorithm for assessing fiber-bundle organization in the human heart using diffusion-tensor magnetic resonance imaging is presented. The proposed approach distinguishes from the locally "greedy" paradigm, which uses voxel-wise seed initialization intrinsic to conventional tracking algorithms. It formulates the fiber tracking problem as the global problem of computing paths in a boolean-weighted undirected graph, where each voxel is a vertex and each pair of neighboring voxels is connected with an edge. This leads to a global optimization task that can be solved by iterated conditional modes-like algorithms or Metropolis-type annealing. A new deterministic optimization strategy, namely iterated conditional modes with α-relaxation using (t_2)- and (t_4)-moves, is also proposed; it has similar performance to annealing but offers a substantial computational gain. This approach offers some important benefits. The global nature of our tractography method reduces sensitivity to noise and modeling errors. The discrete framework allows an optimal balance between the density of fiber bundles and the amount of available data. Besides, seed points are no longer needed; fibers are predicted in one shot for the whole diffusion-tensor magnetic resonance imaging volume, in a completely automatic way. **Magn Reson Med 64:1215–1229, 2010. © 2010 Wiley-Liss, Inc.**

Key words: diffusion tensor MRI; cardiac imaging; fiber tractography; graph theory

Using the properties of water diffusion in the tissues, it is possible to estimate the cardiac muscular organization from diffusion-tensor magnetic resonance imaging (DT-MRI). Water molecules diffuse more easily along the fiber tracts than across them; this anisotropy is captured by the diffusion-weighted MR signal. Tractography methods use the information of directionality contained in diffusion data to infer the fibrous architecture of the human heart. Despite advances in tracking algorithms in DT-MRI, reliable and robust tracking of fibers remains a challenge because of the coarsely sampled and noisy nature of the data.

Streamline tracking algorithms reconstruct fibers incrementally by adding a line segment of a few millimeters in length to the end of the previously added line segment. The direction of the line segment is chosen based on some local function of the data such as the eigenvector with largest eigenvalue of the diffusion tensor (1–3) or the direction maximizing an appropriately constructed Bayesian posterior distribution (4).

Even if perturbations attributable to noise are usually minor at a local scale, the error summation resulting from the incremental and local nature of streamline tracking algorithms may tend to disappointing results. For example, at a voxel scale, an estimate of the eigenvector with largest eigenvalue may differ from the true diffusion direction by perhaps only a few degrees; however, the cumulative effect of a few degrees of error at each of possible thousands of increments can result in a reconstructed trajectory gradually meandering away from the trajectory of the true fiber bundle.

Different methods have been proposed to overcome the limitations of streamline tractography. Probabilistic tracking algorithms (5–7) treat the fiber orientation as a random variable and define a distribution for it. In Ref. 6, the distribution is predicted using simulations, in Ref. 5, it is estimated using Monte Carlo Markov Chain methods, and direct Bayesian inference is used in Ref. 7 to characterize the fiber orientation uncertainty. Trajectories are then generated using Monte Carlo sampling, which results in a set of reconstructed trajectories that do not always reflect reality. In fact, such approaches give an overview of the uncertainty associated with a fiber path seeded in a specific point by producing a map of connection probabilities between each discrete spatial location and the seed. Probabilist tracking algorithms have shortcomings: first, Monte Carlo sampling is computationally expensive, and second, final outputs are spatial distributions rather than single well-defined trajectories, which makes it difficult to further decompose fibers into morphological descriptors for shape analysis.

More recently, global approaches to fiber tracking were proposed. They identify the optimal path between two voxels of interest, according to some global criterion, rather than identifying paths arising from a single voxel. These global approaches are less sensitive to noise. Front propagation techniques (8–11) identify the best paths from a seed to all other voxels by evolving a surface from this seed. The surface front evolves faster along the fiber direction estimates of the underlying tissue. Graph-based tracking algorithms (12,13) formulate fiber tracking as the problem of computing the shortest paths in a weighted digraph, where each voxel is a vertex and edges are pairs of neighboring voxels. These methods exhaustively search for the best path connecting two given voxels of interest. Finally, spin glass models (14,15) parameterize fibers using small segments called spins, which are endowed with several criteria gathered in a global energy.
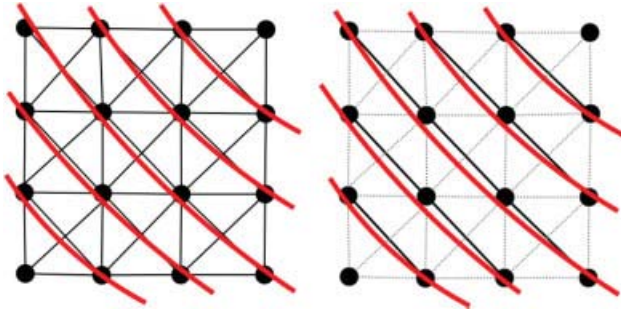
FIG. 1. Left: Representation of the DT volume as a boolean-weighted undirected graph. Fibres to be predicted are displayed in red. Right: Fibre approximation after minimization of the functional. The edges that are parts of fibers have a weight equal to 1 (plain edges) and the others have zero weight (dashed edges). [Color figure can be viewed in the online issue, which is available at wileyonlinelibrary.com.]

The above described approaches were proposed in the context of neurology, where the goal is to find connections between different anatomical brain regions. By contrast, in the context of cardiology, the goal is to segment the whole DT-MRI volume into fiber bundles to estimate the cardiac muscle organization in one shot. Indeed, the motion of the human heart is characterized by the contraction and the relaxation of its intertwining constitutive fibers (16); the spatial organization of cardiac fibers is a fundamental aspect of the overall and segmental heart contractile function.

In this article, we readdress the tractography problem in a global and automatic way that is especially designed for cardiac imaging. Our approach is graph based; vertices are voxels of the diffusion tensor (DT) volume and edges represent the possible connection of two neighboring voxels by a fiber bundle. Starting from a given segmentation of the myocardium, the problem is to select the edges that best correspond to the available data and remove all others by minimizing a global cost functional. Compared with other graph-based tracking algorithms (12,13) (which give the most probable trajectories connecting a seed to a given set of target voxels) our approach is automatic: it produces all the fiber bundles representing a DT-MRI volume, in one shot, with uniform density (one fiber bundle per voxel) and without any seed initialization. Optimization is performed by iterated conditional modes (ICM)-like algorithms and Metropolis-type annealing. A new deterministic optimization strategy, namely ICM with α-relaxation using (t_2)- and (t_4)-moves, is also proposed; it has similar performance to annealing but offers a substantial computational gain.

This article is organized as follows. The next section presents the essential aspects of our graph modeling approach, and we discuss the considered optimization techniques in Section "Optimization". Section "Experimental Setup" describes the elaboration of our synthetic data and the acquisition of our real cardiac data. Our experimental results on synthetic and real data are exposed in Section "Results" and conclusions and perspectives are given in the last section.

GRAPH MODEL

We represent a diffusion tensor volume as a boolean-weighted undirected graph, starting from a given

segmentation of the myocardium in the case of real data. Vertices are voxels of the diffusion tensor volume and edges connect every pair of voxels with respect to a given neighborhood system on the set of vertices of the graph (e.g., the 26-nearest neighbors system). As depicted in Fig. 1, our method selects the edges that best fit the available data by minimizing a cost functional describing the tractography problem in a global way. Let us, respectively, denote by V and E the set of vertices and the set of edges of the graph. The weight of an edge e is denoted by w_e and is either 0 or 1, $w_e = 1$ meaning that e is part of a fiber bundle.

To select the set of edges in the graph that best matches the true fiber bundles, we minimize a cost functional J : $\{0, 1\}^{|E|} \rightarrow \mathbb{R}$ whose argument is the set of weights $w = \{w_e; e \in E\}$ assigned to the edges. This functional is made of two terms: a data-fidelity term and a topological criterion.

Data-Fidelity Term: Compatibility of Edges and Tensors

The role of the data-fidelity term is to favor edges connecting two voxels that are likely to be connected by a fiber bundle. There are two ways to define this term: edge-wise (an edge is compared to two tensors) and vertex-wise (a tensor is compared to two edges). The edge-wise model restricts fiber orientations to edges, which is not always satisfactory as edge orientation possibilities are limited. Therefore, we propose a data-fidelity term based on the vertex-wise model.

Orientation Cost Function

A set of two adjacent edges with common end vertex v defines the tangent of a possible fiber bundle going through v. Given an edge e with end vertices v and w, we denote the vectors $\overrightarrow{vw}$ and $\overrightarrow{wv}$ by $\varepsilon_v(e)$ and $\varepsilon_w(e)$, respectively. The fidelity of a possible diffusion direction at some voxel v is compared to the associated vertex tensor $\mathbf{T}_v$ using the following cost function, which favors the case where the mean orientation of two adjacent edges is aligned with the vertex tensor:

$$M(\mathbf{T}_v, e_1, e_2) = 1 - \frac{\|\mathbf{T}_v \bar{e}\|_2}{\|\bar{e}\|_2 \ \|\mathbf{T}_v\|_2}, \qquad [1]$$

where $\bar{e} = \varepsilon_v(e_1) - \varepsilon_v(e_2)$ represents the mean orientation defined by edges e_1 and e_2 adjacent to vertex v (see Fig. 2), and $\|.\|_2$ is the spectral norm induced by the Euclidean norm ($\|A\|_2 = \sup_{x \neq 0} \frac{\|Ax\|_2}{\|x\|_2}$, which reduces to the largest eigenvalue in modulus when A is symmetric).
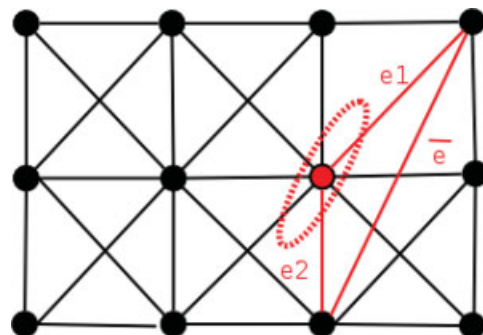

FIG. 2. Tangent-based data-fidelity term. [Color figure can be viewed in the online issue, which is available at wileyonlinelibrary.com.]
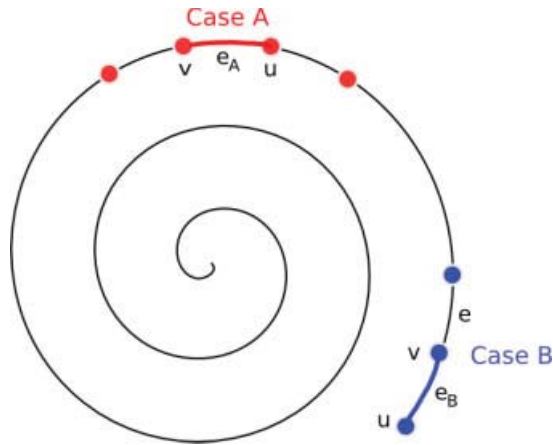
FIG. 3. Data-fidelity term: specific cases considered for the choice of F_1 and F_0 in (3). [Color figure can be viewed in the online issue, which is available at wileyonlinelibrary.com.]

Data Fidelity Term

Let $E(v)$ be the set of edges adjacent to vertex v and let $d(v) = \sum_{e \in E(v)} w_e$. Using the orientation cost function (Eq. [1]), the data-fidelity term F_{data} has the following form:

$$F_{\text{data}}(w) = \sum_{v \in V} F_v(w), \qquad [2]$$

with

$$F_v(w) = \begin{cases} \dfrac{1}{\Gamma_v} \displaystyle\sum_{\substack{\{e_1, e_2\} \subset E(v) \\ \langle \varepsilon_v(e_1), \varepsilon_v(e_2)\rangle < 0}} \\ \qquad \times w_{e_1} w_{e_2} M(\mathbf{T}_v, e_1, e_2) & \text{if } d(v) \geq 2 \\ F_1 & \text{if } d(v) = 1 \\ F_0 & \text{otherwise,} \end{cases} \qquad [3]$$

where the normalization constant Γ_v is given by

$$\Gamma_v = \sum_{\substack{\{e_1, e_2\} \subset E(v) \\ \langle \varepsilon_v(e_1), \varepsilon_v(e_2)\rangle < 0}} w_{e_1} w_{e_2}, \qquad [4]$$

and F_0 and F_1 are positive constants whose choice is discussed in Section "Choice of F_0 and F_1."

The constraint $\langle \varepsilon_v(e_1), \varepsilon_v(e_2)\rangle < 0$ in the summation is meant to enforce cardiac geometrical constraints. When dealing with cardiac data, it is naturally assumed that the centers of connected neighboring voxels are joined by fiber bundles forming circular arcs. Simple geometrical considerations can be used to discriminate arcs whose radius of curvature are not compatible with the human heart architecture (bends). In particular, it is natural to ignore combinations of edges with angle smaller than $\pi/2$.

Topological Criterion and Global Cost

There exist many configurations in the graph that cannot correspond to true fiber bundles. In particular, histological studies have shown that crossings do not occur in the human left ventricle (17). We can therefore add a criterion to specify that the graph is composed of lineic objects. An efficient way to introduce such prior information at a

local level is to encourage each vertex to be connected to at most two neighbors. This is done by means of the following topological cost function:

$$F_{\text{topo}}(w) = \sum_{v \in V} \Phi_v(w), \qquad [5]$$

where

$$\Phi_v(w) = \begin{cases} d(v) - 2 & \text{if } d(v) > 2 \\ 0 & \text{otherwise.} \end{cases} \qquad [6]$$

Then, the global cost functional characterizing our problem is given by

$$J : w \in \{0,1\}^{|E|} \mapsto F_{\text{data}}(w) + \alpha F_{\text{topo}}(w), \qquad [7]$$

where, depending on the optimization technique, the parameter α is either set to 1 [classical ICM and simulated annealing (SA)], or gradually increased during the minimization process [ICM with α-relaxation].

Choice of F_0 and F_1

The specific values F_0 and F_1 taken by $F_v(w)$ (Eq. [3]) when the vertex degree $d(v)$ is equal to 0 or 1 are meant to deal with the two cases depicted in Fig. 3: (a) "cutting inside the fiber" and (b) "cutting off a fiber extremity." More specifically, a fiber should not be cut into two parts because one tensor on the fiber trajectory is inaccurate, while fiber extremities have to be cut off when the tensor is too noisy in order to prevent erroneous fiber terminations and border effects. This is particularly true for real cardiac data. Indeed, because we apply a mask to our graph to segment the myocardium from the background, it may happen that some voxels of the background are not removed, which leads to unrealistic fiber terminations as shown in Fig. 4.

Let $\Delta(e)$ be the energy variation observed when setting the weight of an edge e to zero. We have

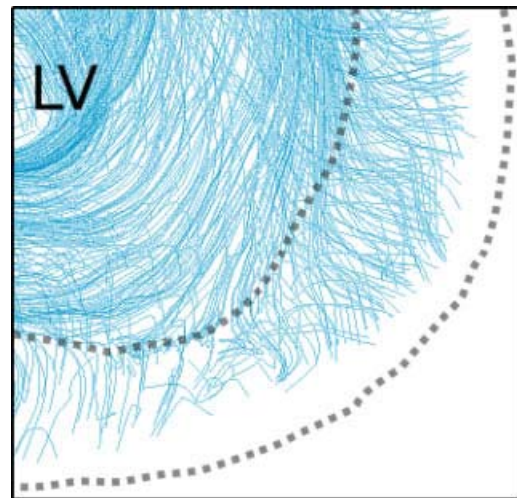$$\Delta(e) = F_u(w_0) - F_u(w_1) + F_v(w_0) - F_v(w_1), \qquad [8]$$

FIG. 4. Unrealistic fiber terminations from real cardiac data (region encircled by dashed lines). LV stands for left ventricle. [Color figure can be viewed in the online issue, which is available at wileyonlinelibrary.com.]
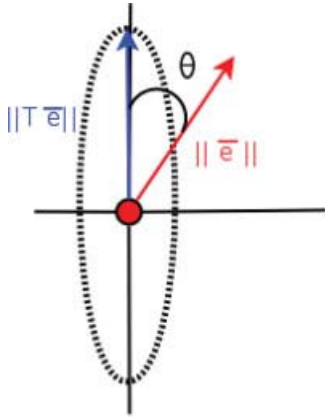
FIG. 5. Error angle between the fiber tangent and the tensor. [Color figure can be viewed in the online issue, which is available at wileyonlinelibrary.com.]

where u and v are the end vertices of e, w_1 is the set of weights before setting w_e to zero, and w_0 is the set of weights after setting w_e to zero. For cases A and B depicted in Fig. 3, this writes

$$\Delta(e_A) = 2F_1 - (F_u(w_1) + F_v(w_1)),$$
$$\Delta(e_B) = F_0 - F_v(w_1). \qquad [9]$$

For case A, the nonconnected case $w(e_A) = 0$ should never be preferred to the connected case $w(e_A) = 1$, that is, we should have $\Delta(e_A) \geq 0$, which suggests to set $F_1 = 1$ (the maximal value of $F_v(w)$).

For case B, we should favor the nonconnected case when the orientation cost $M(\mathrm{T}_v, e_B, e)$ exceeds a certain threshold F_0. In this situation, we should have $F_v(w_1) \geq F_0$. The orientation cost $M(\mathrm{T}_v, e_B, e)$ can be associated to an error angle θ between the fiber tangent and the tensor. Let us assume that the tensor $\mathbf{T}_v$ is highly anisotropic so that $\mathbf{T}_v \bar{e}$ corresponds approximatively to the projection of $\bar{e}$ on the principal direction of the tensor $\mathbf{T}_v$ (see Fig. 5). In this case,

$$\cos \theta \approx \frac{\|\mathbf{T}_v \bar{e}\|_2}{\|\bar{e}\|_2 \|\mathbf{T}_v\|_2}. \qquad [10]$$

From definitions (1) and (3), it follows that

$$F_v(w_1) \approx 1 - \cos \theta \qquad [11]$$

and hence we should have

$$F_0 \leq 1 - \cos \theta. \qquad [12]$$

Therefore, the constant F_0 can be interpreted as a cutting angle. To select an appropriate value for F_0, we simply have to fix the maximal error angle to be tolerated at a fiber termination. Because our graph is supported by a 3D regular voxel lattice with at least 26-nearest neighbor connectivity, $\frac{\pi}{4}$ is a fair compromise, so that we finally set $F_0 = 1 - \frac{1}{\sqrt{2}}$.

The above choices for the values of the thresholds F_0 and F_1 are adapted to cardiomyopathies and cardiac tumors because a fibrous structure subsists in these cases. [The myocardial fibers are disarrayed in orientation in the case of cardiomyopathies (18) and often run through the tumoral mass in the case of cardiac tumors (e.g., fibromas (19)).]

OPTIMIZATION

Minimizing the cost function J (Eq. [7]) is a challenging optimization task, as J typically exhibits numerous local minima. In this context, stochastic optimization techniques like SA have shown good performance for many computer vision applications [see, e.g., (20)]. Annealing is a dynamic Monte Carlo method controlled by a temperature parameter inspired by physical annealing processes (21). In the zero temperature limit, Metropolis-type SA boils down to the popular deterministic optimization algorithm known as ICM (22). In practice, SA is generally much slower than deterministic approaches and it is thus important to assess the benefits associated with SA. In this section, we propose an improved ICM-like algorithm, and we discuss the implementation of SA to minimize J. The relative performance of the two methods is compared in the experimental section.

Optimization by ICM

A straightforward application of ICM to the minimization of the cost function J is to update one edge at each iteration. This simple updating strategy is repeatedly iterated over all edges of the graph in a quasi-random manner, and the visit of all the edges of the graph is called a sweep. The algorithm is run until convergence, that is, until no edge weight is changed during one sweep. Indeed, at each iteration, the current edge weight is assigned to the value that gives the smallest cost; therefore, the cost function decreases at each iteration and, because the state space $\{0, 1\}^{|E|}$ is finite, it is guaranteed that ICM converges in a finite number of iterations.

Updating Strategies

The energy landscape defined by a single-edge flip strategy has many poor local minima that are likely to trap the ICM algorithm. Consequently, it is interesting to introduce larger moves in the configuration space to reduce the number of irrelevant minima and hence to increase the chance of ICM to produce good solutions. We consider the three updating schemes described below.

Single-edge Moves (t_1). This is the simplest updating scheme: it flips the value of one edge weight at a time under the condition that the cost function does not increase.

Edge-pair Moves (t_2). This scheme operates on pairs of edges sharing an end vertex. Given such a pair of edges, it selects the weighting configuration that leads to the smaller value of the cost function. Examples of such flips are depicted in Fig. 6. (Note that (t_1)-moves belong to the set of (t_2)-moves).

Crossing Scheme (t_4). This updating scheme is meant to avoid the fiber crossings that are observed in the local minima obtained with single-edge flips. The corresponding moves are illustrated in Fig. 7: a fiber crossing (i.e., two intersecting edges with weight 1) is replaced by parallel fibers (i.e., two parallel edges with weight 1) whenever it leads to a smaller value of the cost function.

Optimization by SA

At each iteration of SA, a new candidate solution y is generated from the current solution x by drawing from a
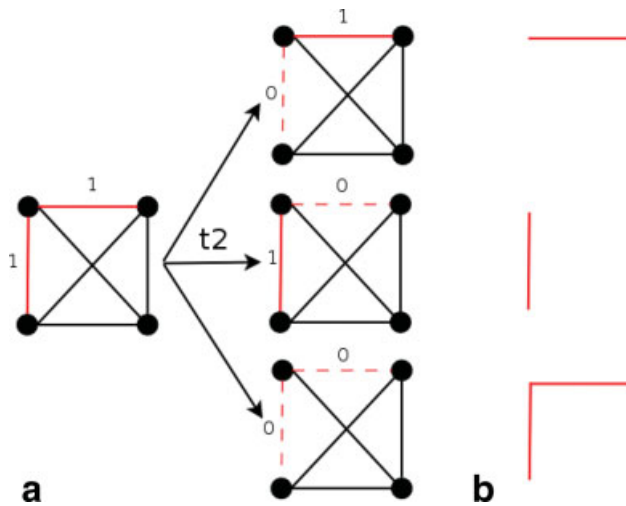
FIG. 6. **a**: Possible transitions from connected to nonconnected vertices with a t_2 updating scheme; **(b)** corresponding flip possibilities. [Color figure can be viewed in the online issue, which is available at wileyonlinelibrary.com.]

probability distribution $q(x,.)$ defined by a Markov matrix q on E. Then, y becomes the current solution if its energy is smaller than the energy of x. Otherwise, if the energy of y is greater than the energy of x, then y becomes the current solution with a probability, which decreases with the energy difference and increases with temperature. The temperature is gradually decreased so that nearly any move is accepted during the first iterations, whereas most "uphill" moves are discarded by the end of the annealing process. Roughly speaking, the possibility to move "uphill" prevents SA from being stuck in poor local minima and SA behaves similar to ICM at low temperatures.

Let Ω denote the configuration space $\{0,1\}^{|E|}$ and let $q : \Omega^2 \to [0,1]$ be a symmetric and irreducible Markov kernel on Ω called the communication kernel. The communication kernel specifies how to generate a new candidate solution from the current one. It is usually defined by selecting a neighborhood system $\mathcal{N}(\Omega) = \{\mathcal{N}_w(\Omega) : w \in \Omega\}$ and setting

$$q(w,x) = \begin{cases} |\mathcal{N}_w(\Omega)|^{-1} & \text{if } x \in \mathcal{N}_w(\Omega), \\ 0 & \text{otherwise.} \end{cases} \quad [13]$$

For any $\beta \in \mathbb{R}_+^*$, define the transition probability matrix P_β on Ω by

$$P_\beta(w,x) = \begin{cases} q(w,x)\exp(-\beta(J(x)-J(w))^+) & \text{if } x \neq w, \\ 1 - \sum_{z \in \Omega \setminus \{w\}} P_\beta(w,z) & \text{otherwise,} \end{cases} \quad [14]$$

where $a^+ := \max\{a,0\}$, and let $(\beta_n)_{n\in\mathbb{N}^*}$ be a nondecreasing positive real sequence called the cooling schedule $[(\beta_n)_n$ is a sequence of inverse temperatures]. A Metropolis-type annealing algorithm to minimize J is a discrete-time nonhomogeneous Markov chain $(X_n)_{n\in\mathbb{N}^*}$ with transitions $P(X_n = x|X_{n-1} = w) = P_{\beta_n}(w,x)$. Under our assumptions, P_β is irreducible and aperiodic. Its unique equilibrium probability measure is the Gibbs distribution π_β with energy J and temperature β^{-1}: $\pi_\beta(w) = Z^{-1}\exp(-\beta J(w))$, where Z is a normalizing constant. One can check that π_β tends to

the uniform distribution on the set $\Omega_{\min}$ of global minima of J as β goes to infinity. Hence, the key idea of annealing is that, for sufficiently slowly increasing cooling schedules, the law of X_n should be close to π_{β_n} and, consequently, one can expect that

$$\lim_{n\to\infty} \inf_{w\in\Omega} P(X_n \in \Omega_{\min}|X_0 = w) = 1. \quad [15]$$

Early results show that this desirable property holds for suitably adjusted logarithmic schedules (23–25). However, it is demonstrated in (26) that exponential cooling must be preferred as soon as one deals with a finite amount of computing time. We use exponential cooling schedules of the form

$$\beta_n = \beta_{\min}\left(\frac{\beta_{\max}}{\beta_{\min}}\right)^{\frac{n}{N}}, \quad [16]$$

where $\beta_{\min}$ and $\beta_{\max}$, respectively, denote the initial and final inverse temperature values, and N is the length of the annealing chain. The selection of $\beta_{\min}$ and $\beta_{\max}$ is performed according to the methods proposed in (27) in the context of image reconstruction.

Communication Kernels

In our experiments, we will consider two different communication mechanisms q_1 and q_2 of the form (Eq. [13]) corresponding, respectively, to single-edge moves and edge-pair moves. Let $\zeta(x,w) = \{e \in E | x_e \neq w_e\}$ denote the set of edges, where x and w differ. The associated neighborhood systems $\mathcal{N}_{1,w}(\Omega)$ and $\mathcal{N}_{2,w}(\Omega)$ are defined as follows.

Single-edge Moves (q_1). $\mathcal{N}_{1,w}(\Omega)$ is the set of configurations $x \in \Omega$ that differ from w only at one edge:

$$\mathcal{N}_{1,w}(\Omega) = \{x \in \Omega \mid |\zeta(x,w)| = 1\}. \quad [17]$$

Edge-pair Moves (q_2). $\mathcal{N}_{2,w}(\Omega)$ is the set of configurations $x \in \Omega$ that differ from w at most two edges sharing an endvertex. In other words, $\mathcal{N}_{2,w}(\Omega)$ is the set of configurations $x \in \Omega$ such that

$$\begin{cases} |\zeta(x,w)| \leq 2 \\ \text{If } \zeta(x,w) = \{e_1,e_2\} \text{ with } e_1 \neq e_2, \text{ then } e_1 \text{ and} \\ \quad e_2 \text{ share an end vertex.} \end{cases} \quad [18]$$
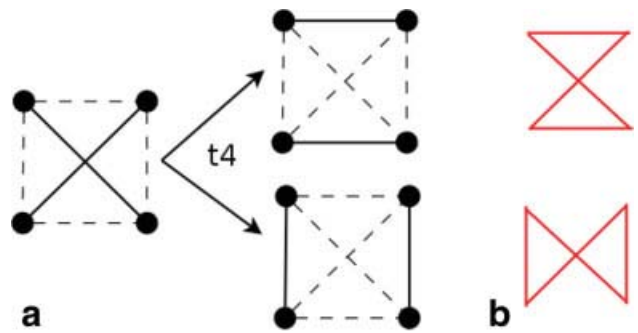

FIG. 7. **a**: Possible transitions from connected to nonconnected vertices with a t_4 updating scheme; **(b)** corresponding flip possibilities. [Color figure can be viewed in the online issue, which is available at wileyonlinelibrary.com.]
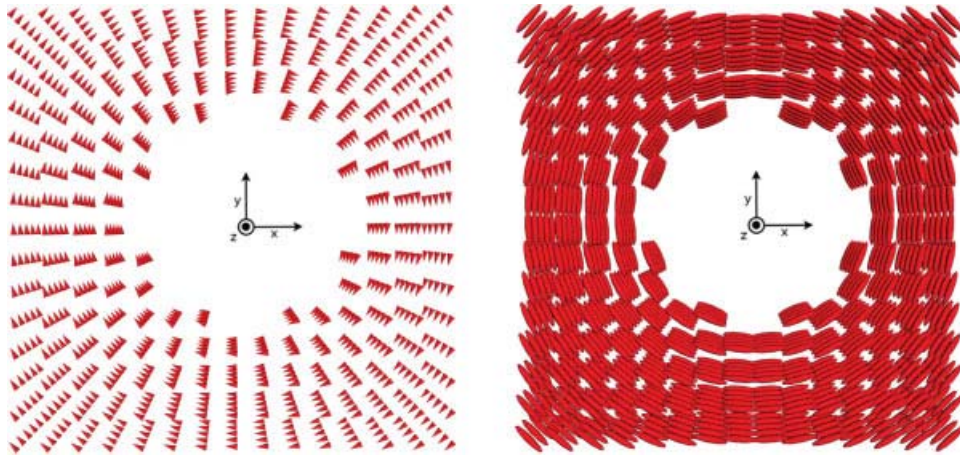
FIG. 8. Left: Principal direction field associated with the synthetic cylindrical dataset. Right: DT field associated with the synthetic cylindrical dataset.

EXPERIMENTAL SETUP

Synthetic Data

Computer-generated data allow accurate error analysis and targeted testing of specific fiber characteristics, as the precise trajectory of the fibers to be tracked is known in advance. We generated an artificial principal direction field ϕ with cylindrical shape and size $15 \times 15 \times 5$. The field is depicted in Fig. 8, and the corresponding expression in polar coordinates is

$$\phi(\rho, \theta, z) = \begin{cases} (\sin\theta, -\cos\theta, 0) \text{ if } \rho \geq \rho_{\min} \\ (0, 0, 0) \text{ otherwise.} \end{cases} \quad [19]$$

The associated DT field is given by

$$T(x, y, z) = v_1 v_1^T + \kappa \left(v_2 v_2^T + v_3 v_3^T \right) \quad [20]$$

with $v_1 = \phi(x, y, z)$, $v_2 = (0, 0, 1)$, $v_3 = v_1 \wedge v_2$, and $\kappa \in (0, 1)$. Putting it another way,

$$T(x, y, z) = R \Lambda R^T, \quad [21]$$

where Λ is the 3×3 diagonal matrix with coefficients $(0, \kappa, \kappa)$ and R is the 3×3 orthogonal matrix whose columns are the coordinates of v_1, v_2, and v_3.

We used the Stejskal-Tanner diffusion equations to compute the DW images associated with T. The corresponding MR measurement without diffusion sensitization was chosen to be constant, and we considered the cuboctahedron encoding scheme (six directions) to simulate the gradient sequence. Several rician noises with different standard deviation values were added to the "ideal" DW volumes. The resulting sequences of noisy DW volumes were used to estimate a discrete DT field using least-squares estimation. Figure 9 shows examples of simulated DW volumes together with the corresponding synthetic DT fields.
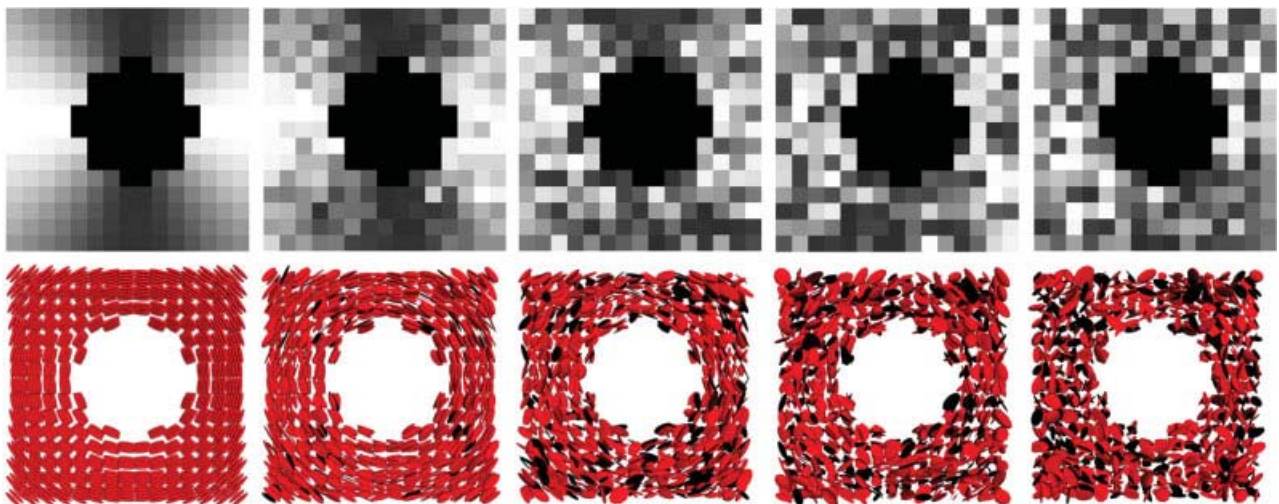

FIG. 9. Slices of the simulated DW volumes and associated DT fields with increasing noise standard deviation (from $\sigma = 0$ to $\sigma = 1.2$ with a constant step of 0.3). The encoding gradient related to the DW image is $G = 1/\sqrt{2}\,(1, 0, 1)$.

FIG. 10. Fibre tract estimations from the synthetic dataset using the streamlining approach. The displayed fibers have length greater than 50 mm. Left to right: Increasing noise level from $\sigma = 0$ (PSNR = $+\infty$) to $\sigma = 1.2$ (PSNR = 4.4 dB) with a constant step of 0.3. Top to bottom: Integration steps (0.1 and 1) for the Runge-Kutta integration scheme. [Color figure can be viewed in the online issue, which is available at wileyonlinelibrary.com.]

Real Data

We studied 16 ex vivo human hearts from healthy to severely diseased. Each heart was placed in a plastic container filled with hydrophilic gel to maintain diastolic shape. The data were acquired with a Siemens Avanto 1.5 T MR Scanner. Diffusion images were obtained using an echo planar imaging pulse sequence with the following parameters: 128×128 image size, $2 \times 2 \times 2$ mm^3 resolution, and 52 contiguous axial slices. The DT-MRI acquisition protocol is generally defined by the number N_d of diffusion-sensitizing directions and the number N_e of excitations used for signal averaging. In this work, $(N_d, N_e) = (12, 4)$ was selected among other combinations in agreement with the comparison of the acquisition protocols conducted in (28). The acquisition time for a 3D dataset is about 7–8 min.

RESULTS

Synthetic Data

We applied our global tractography approach and the streamlining approach on the synthetic dataset corrupted by Rician noise with peak signal-to-noise ratio (PSNR) ranging from $+\infty$ to 1 dB (which corresponds to $\sigma \in [0, 1.5]$); the PSNR is defined by

$$\text{PSNR} = 10 \cdot \log_{10}\left(\frac{|V| \, \Delta f^2}{\|d - f\|_2^2}\right), \qquad [22]$$

where Δf is the voxel value range, $\|.\|_2$ is the standard Euclidean norm, and $|V|$ is the number of vertices (each vertex is associated to a voxel). The methods are compared quantitatively by means of specific measures, namely mean fiber length, fiber-length dispersion, fiber number, and fiber error, the precise definition of which is given in Section Quantitative Analysis. Note that both approaches are implemented in C and were run on a standard (2.66 GHz, 2 Gb RAM) PC.

In the case of our approach, we consider the sets of edges defined by the 26- and the 124-nearest neighbor systems. More specifically

$$E = \{\{v, v'\} \subset V \mid v' \in \mathcal{N}_v(V)\}$$

with $\mathcal{N}_v(V) = \{v' \in V \mid \|v' - v\|_2 \leq \sqrt{3}\}$ (26-connectivity)

or $\mathcal{N}_v(V) = \{v' \in V \mid \|v' - v\|_\infty \leq 2\}$ (124-connectivity),

where $\|.\|_2$ and $\|.\|_\infty$, respectively, stand for the ℓ_2- and the ℓ_∞ norm.

Qualitative Analysis

Figures 10–12 show the estimation of fiber tracts from the synthetic cylindrical dataset using our graph-based approach with 26 and 124 connectivities and using the streamlining approach. The streamlining approach (Fig. 10) was run with integration steps of 0.1 and 1. The criteria for stopping the tracking are thresholds on fractional anisotropy (FA ≤ 0.08) and on curvature (to avoid highly bended fibers, the angle between two successive principal directions is kept smaller than 20°.). The results associated with the graph-based approach (Figs. 11 and 12) were obtained using (a) ICM with a fixed value of the parameter α in (Eq. [7]) [$\alpha = 1$] and edge-pair moves, (b) ICM with gradual increase of α and both edge-pair moves and "crossing scheme" moves, and (c,d) SA with edge-pair moves. The results associated with single-edge moves are not as good; they are not displayed here.

When using the proposed graph-based approach, some fibers may deviate from the expected trajectory even for low noise levels; this effect is less pronounced in the case of streamlining. However, the fiber density obtained with our approach is more robust to noise.

Quantitative Analysis

Graph Energy. Tables 1 and 2 give the mean energy per vertex $J/|V|$ obtained with our approach using different optimization strategies in the case of 26- and 124-connectivity.

Compared to standard ICM, the Metropolis-type annealing algorithm produces configurations with substantially lower energies and hence better approximations of the
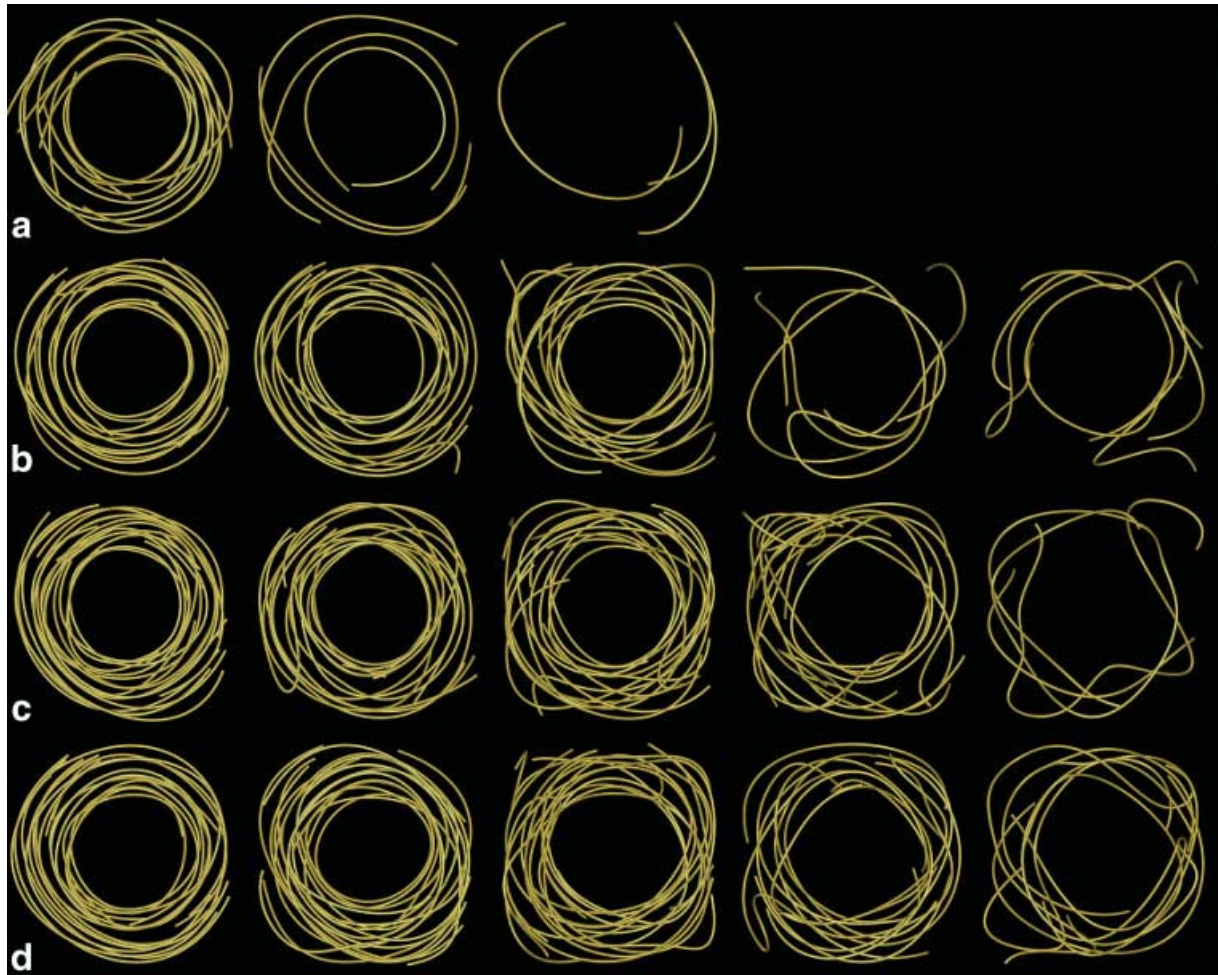
FIG. 11. Fibre tract estimations from the synthetic dataset using our approach with 26-connectivity (6523 edges). The displayed fibers have length greater than 50 mm. Left to right: Increasing noise level from $\sigma = 0$ (PSNR $= +\infty$) to $\sigma = 1.2$ (PSNR $= 4.4$ dB) with a constant step of 0.3. Top to bottom: Optimization techniques: (**a**) ICM with $\alpha = 1$ using (t_2)-moves, (**b**) ICM with α-relaxation using (t_2)- and (t_4)-moves, (**c**) SA with communication q_2 and $8000|E|$ iterations, and (**d**) SA with communication q_2 and $64,000|E|$ iterations. [Color figure can be viewed in the online issue, which is available at wileyonlinelibrary.com.]

global fibrous structure according to our model. Note that increasing the number of iterations for Metropolis-type annealing gives better estimates but is obviously more time consuming. We also observe that the use of larger moves in the minimization process (i.e., (t_2)-moves rather than (t_1)-moves in the case of ICM and communication of type q_2 rather than q_1 in the case of annealing) produces deeper minima. In other words, changing the weights of several edges simultaneously improves the convergence rate.

ICM with α-relaxation outperforms standard ICM and sometimes SA; this is particularly true when using both (t_2)- and (t_4)-moves. Indeed, α-relaxation allows gradual increase of the complexity of the minimization problem, which avoids being trapped in poor local minima. Furthermore, the proposed deterministic optimization strategy (ICM with α-relaxation using (t_2)- and (t_4)-moves) performs better than SA with $16,000|E|$ iterations in the case of 26-connectivity when the PSNR is high ($\sigma < 0.6$) (the corresponding computational gain is $\frac{46}{6} \approx 7.66$). It performs better than SA with $64,000|E|$ iterations in all cases when considering 124-connectivity (which gives a

computational gain of $\frac{259}{6} \approx 43.16$). This last observation shows that the proposed modified ICM algorithm is less sensitive than SA to the increase in complexity associated with higher connectivity.

As far as the final energy level is concerned, these results suggest that one should favor the proposed modified ICM algorithm in the case of high SNR and SA in the case of low SNR.

Mean Fiber Length. Figure 13 displays the mean fiber length for the whole fiber population as a function of the noise level using streamlining and using the proposed graph-based approach. Our approach gives fibers with greater length than does streamlining with an integration step of 1 (for all noise levels) and streamlining with an integration step of 0.1 when the PSNR is smaller than 32 dB. From a PSNR point of view, it is the area from 20 to 10 dB that is meaningful in terms of real data quality. Similar results are obtained with 124-connectivity.

In the case of streamlining, the mean fiber length drastically decreases as the noise level increases in the low PSNR
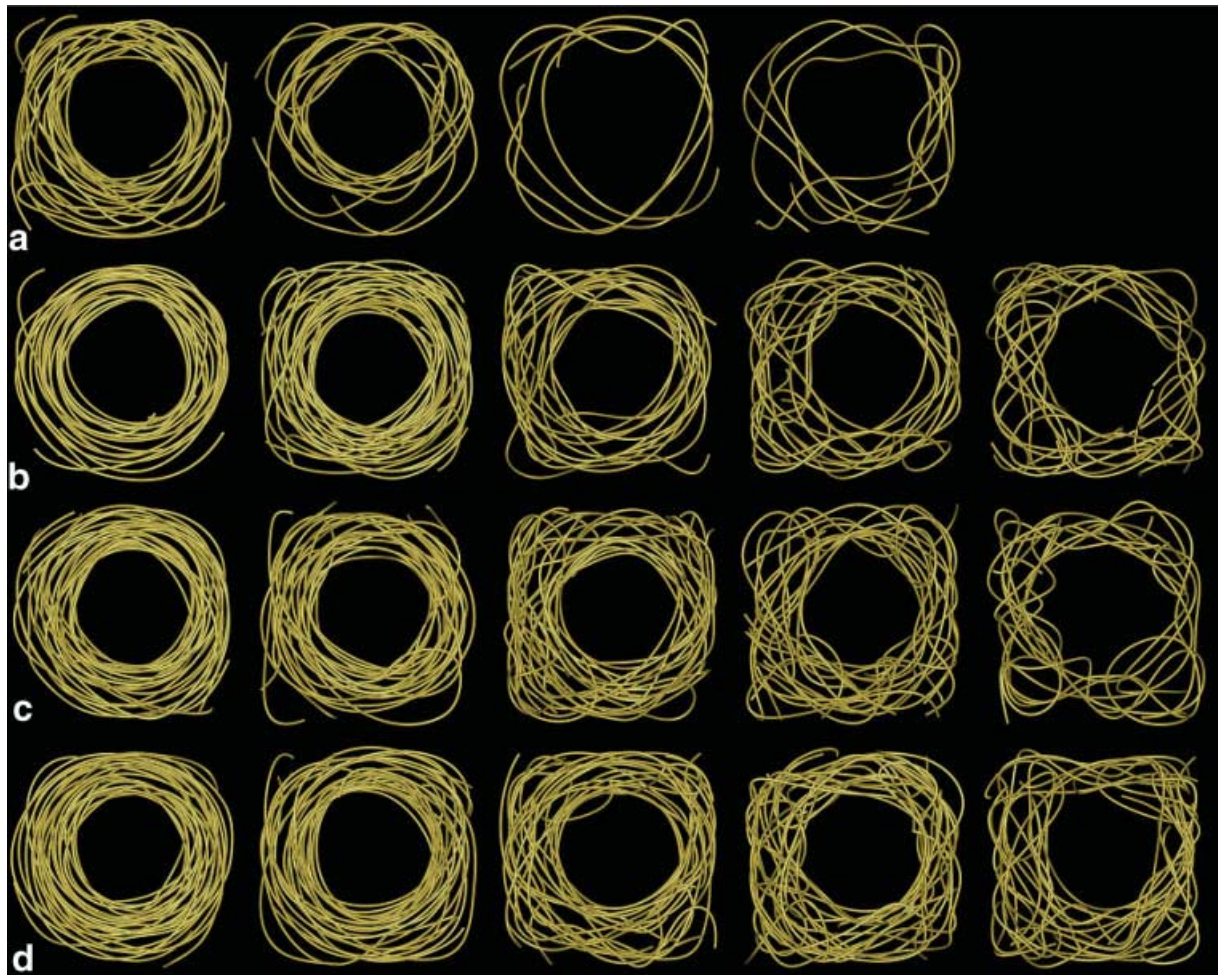
FIG. 12. Fibre tract estimations from the synthetic dataset using our approach with 124-connectivity (22,829 edges). The arrangement is the same as in Fig. 11. [Color figure can be viewed in the online issue, which is available at wileyonlinelibrary.com.]

region. This high sensitivity to noise is due to the fact that the termination of fiber tracts depends on the fractional anisotropy and on the curvature angle whose accuracy is highly noise dependent. Our approach presents more stable mean fiber length thanks to the topological term, which enforces each vertex to be connected to at most two neighbors and thus tends to produce fibers with similar lengths independently of the noise level.

Table 1
Energies and Computation Times Associated with Fibre Tract Estimations Obtained from the Synthetic Dataset with our Approach Using 26-Connectivity

	Method	Comp. time	$\sigma = 0$	$\sigma = 0.3$	$\sigma = 0.6$	$\sigma = 0.9$	$\sigma = 1.2$
t_1	ICM	1	0.549	0.550	0.568	0.572	0.582
	SA (8000$|E|$)	16	0.344	0.406	0.482	0.526	0.547
q_1	SA (16,000$|E|$)	30	0.334	0.397	0.475	0.522	0.546
	SA (32,000$|E|$)	56	0.323	0.390	0.466	0.508	0.544
	SA (64,000$|E|$)	115	0.311	0.383	0.461	0.511	0.541
t_2	ICM	2	0.446	0.480	0.505	0.512	0.524
	SA (8000$|E|$)	24	0.317	0.399	0.452	0.476	0.499
q_2	SA (16,000$|E|$)	46	0.305	0.390	0.444	0.469	0.490
	SA (32,000$|E|$)	88	0.301	0.383	0.438	0.462	0.478
	SA (64,000$|E|$)	170	0.295	0.376	0.434	0.458	0.472
t_1	ICM	3	0.341	0.426	0.494	0.537	0.556
t_2	+	4	0.308	0.393	0.454	0.490	0.501
$t_2 \bigcup t_4$	relaxation	6	0.304	0.387	0.445	0.463	0.485

The computation time is divided by the computation time corresponding to ICM with $\alpha = 1$ and (t_1)-moves.

Table 2
Energies and Computation Times Associated with Fiber Tract Estimations Obtained from the Synthetic Dataset with our Approach Using 124-Connectivity

	Method	Comp. time	$\sigma = 0$	$\sigma = 0.3$	$\sigma = 0.6$	$\sigma = 0.9$	$\sigma = 1.2$
t_1	ICM	1	0.552	0.573	0.588	0.591	0.595
	SA (8000$|E|$)	29	0.374	0.414	0.446	0.476	0.484
q_1	SA (16,000$|E|$)	55	0.357	0.400	0.436	0.459	0.472
	SA (32,000$|E|$)	105	0.344	0.392	0.423	0.447	0.460
	SA (64,000$|E|$)	209	0.336	0.385	0.412	0.438	0.449
t_2	ICM	3	0.428	0.471	0.509	0.525	0.534
	SA (8000$|E|$)	35	0.355	0.401	0.437	0.459	0.476
q_2	SA (16,000$|E|$)	69	0.339	0.385	0.421	0.448	0.463
	SA (32,000$|E|$)	130	0.321	0.371	0.407	0.433	0.446
	SA (64,000$|E|$)	259	0.303	0.359	0.395	0.421	0.438
t_1	ICM	3	0.348	0.398	0.441	0.473	0.495
t_2	+	4	0.290	0.355	0.394	0.430	0.445
$t_2 \bigcup t_4$	relaxation	6	0.284	0.346	0.389	0.420	0.436

The computation time is divided by the computation time corresponding to ICM with $\alpha = 1$ and (t_1)-moves.

Fibre-length Dispersion. The fiber-length dispersion is defined as the ratio of the fiber-length standard deviation to the mean fiber length.

Figure 14 displays the fiber-length dispersion for the whole fiber population as a function of the noise level using streamlining and using the proposed graph-based approach. For all noise levels and all optimization strategies, our approach produces fibers with lower length dispersion than does streamlining. Similar results are obtained when considering 124-connectivity.

The fiber-length dispersion gradually decreases as the noise level increases. In the case of streamlining, the fiber-length dispersion is high because of the cohabitation of long fibers (accurate fiber tract estimations) with short ones that appear near the mask boundaries. When the noise level is high, long fibers are less numerous and the number of short fibers is higher as the noise corrupts the fractional anisotropy and the curvature angle, which are used as termination criteria. By comparison, our approach presents more stable dispersion, which is again a consequence of the topological term. The SA algorithm produces solutions with higher fiber-length dispersion than those obtained with ICM. Yet, this observation must be put into perspective as SA leads to significantly longer fibers.

Number of Fibers. Tables 3 and 4 display the number of fibers estimated using streamlining with different integration steps and using the proposed graph-based approach in the case of 26-connectivity (the results are similar in the case of 124-connectivity). Fibres with length smaller than 4 mm were not taken into account. Besides, in the case of streamlining, the number of seeds is equal to the number of voxels, and redundant fibers are removed (our graph-based approach does not produce redundant fibers).
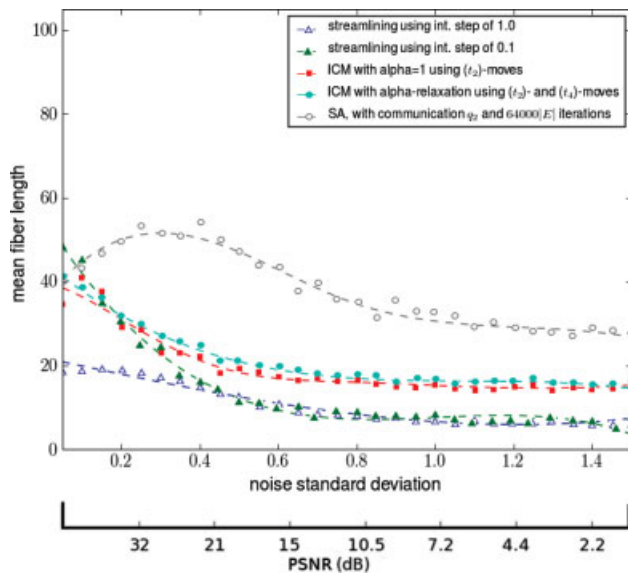

FIG. 13. Mean fiber length associated with fiber tract estimations obtained from the synthetic dataset with our approach using 26-connectivity and with the streamlining approach. [Color figure can be viewed in the online issue, which is available at wileyonlinelibrary.com.]
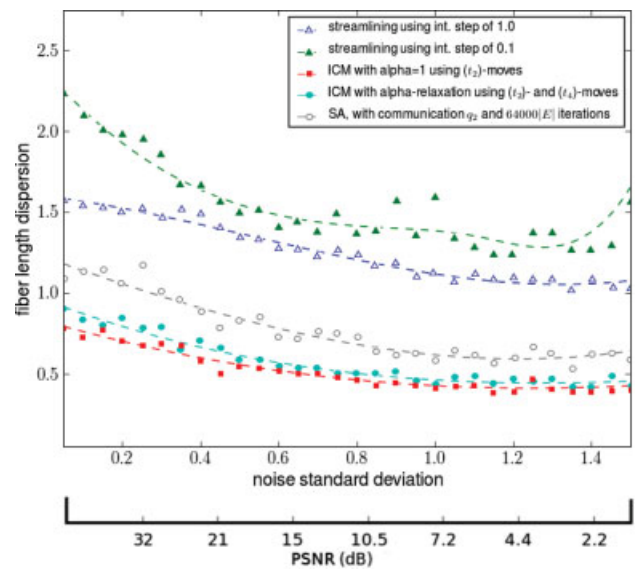

FIG. 14. Fiber-length dispersion associated with fiber tract estimations obtained from the synthetic dataset with our approach using 26-connectivity and with the streamlining approach. [Color figure can be viewed in the online issue, which is available at wileyonlinelibrary.com.]

Table 3

Number of Fibers Associated with Fiber Tract Estimations Obtained from the Synthetic Dataset with our Approach Using 26-Connectivity

	Method	$\sigma = 0$	$\sigma = 0.6$	$\sigma = 1.2$	Evolution (%)
t_1	ICM	68	82	90	32.3
	SA (8000$|E|$)	30	34	38	26.7
q_1	SA (16,000$|E|$)	28	31	34	21.4
	SA (32,000$|E|$)	24	26	29	17.8
	SA (64,000$|E|$)	22	24	25	13.6
t_2	ICM	62	75	80	29.1
	SA (8000$|E|$)	26	29	32	23.1
q_2	SA (16,000$|E|$)	24	27	29	20.8
	SA (32,000$|E|$)	22	23	25	15.6
	SA (64,000$|E|$)	20	20	21	5
t_1	ICM	45	49	55	22.2
t_2	+	38	40	44	15.7
$t_2 \bigcup t_4$	relaxation	35	37	39	11.4

Compared to standard ICM, Metropolis-type annealing produces less fibers (increasing the number of iterations of SA further reduces this number). This is a consequence of our global model, which favors configurations with long fibers and where only one fiber goes through any given voxel.

As regards the influence of the noise term, we observe that both approaches (streamlining and graph-based) produce more fibers as the noise level increases. When the PSNR is 4.4 dB ($\sigma = 1.2$), streamlining gives more than twice the number of fibers obtained in the absence of noise. By contrast, using our approach, the number of additional fibers is about 5% only in the case of SA with communication q_2 and $64,000|E|$ iterations and about 11% in the case of our modified ICM algorithm (α-relaxation and (t_2)+(t_4)-moves). This shows that streamlining is much more sensitive to noise than is our approach when considering the number of predicted fibers. It is due to noisy estimations of the fractional anisotropy and of the curvature angle, which results in unreliable and erroneous terminations of the tractography process.

Fiber Error. To assess the accuracy of a tracking algorithm, we can measure the adequation of the reconstructed fibers $\phi_i : [0, L] \longrightarrow \mathbb{R}^3$ to the noise-free tensor distribution by computing the error term

$$\mathcal{E}(\phi_i) = \frac{1}{L(\phi_i)} \int_0^L \left(1 - \frac{\left\| \mathbf{T}_v(\phi_i(l))\, \phi_i'(l) \right\|_2}{\left\| \phi_i'(l) \right\|_2 \left\| \mathbf{T}_v(\phi_i(l)) \right\|_2} \right) \left\| \phi_i'(l) \right\|_2 \, dl,$$

[23]

where $L(\phi_i) = \int_0^L \|\phi_i'(l)\|_2 \, dl$ denotes the length of ϕ_i, $\mathbf{T}_v(\phi_i(l))$ is the tensor at $\phi_i(l)$, and $\|.\|_2$ is the spectral norm induced by the Euclidean norm $\|.\|_2$.

Figure 15 displays the mean error per fiber (for the whole fiber population) as a function of the noise level

Table 4

Number of Fibers Associated with Fiber Tract Estimations Obtained from the Synthetic Dataset with the Streamlining Approach

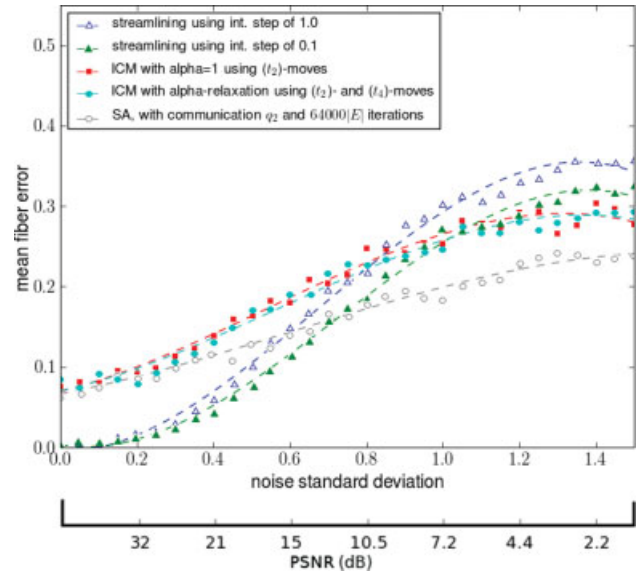|	Int. step	$\sigma = 0$	$\sigma = 0.6$	$\sigma = 1.2$	Evolution (%)
Steamlining	0.1	245	585	602	145
	1.0	244	451	499	104

FIG. 15. Fiber error associated with fiber tract estimations obtained from the synthetic dataset with our approach using 26-connectivity and with the streamlining approach. [Color figure can be viewed in the online issue, which is available at wileyonlinelibrary.com.]

using streamlining with different integration steps and using the proposed graph-based approach with different optimization strategies in the case of 26-connectivity.

For high PSNR, streamlining performs better than our approach regarding this specific measure as the propagation of line segments stops when the fractional anisotropy becomes too low (and hence when the mean fiber error becomes too large). However, this observation does not take the fiber length into account, which is crucial to assess fiber likelihood. By contrast, our approach promotes
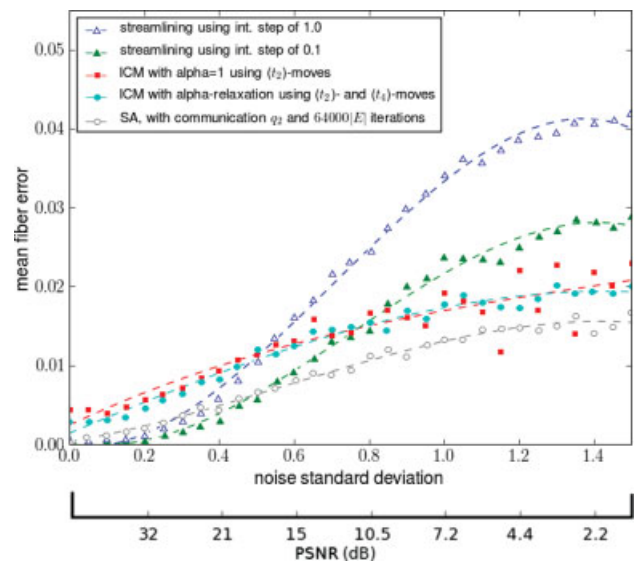

FIG. 16. Weighted fiber error (Eq. [24]) associated with fiber tract estimations obtained from the synthetic dataset with our approach using 26-connectivity and with the streamlining approach. [Color figure can be viewed in the online issue, which is available at wileyonlinelibrary.com.]
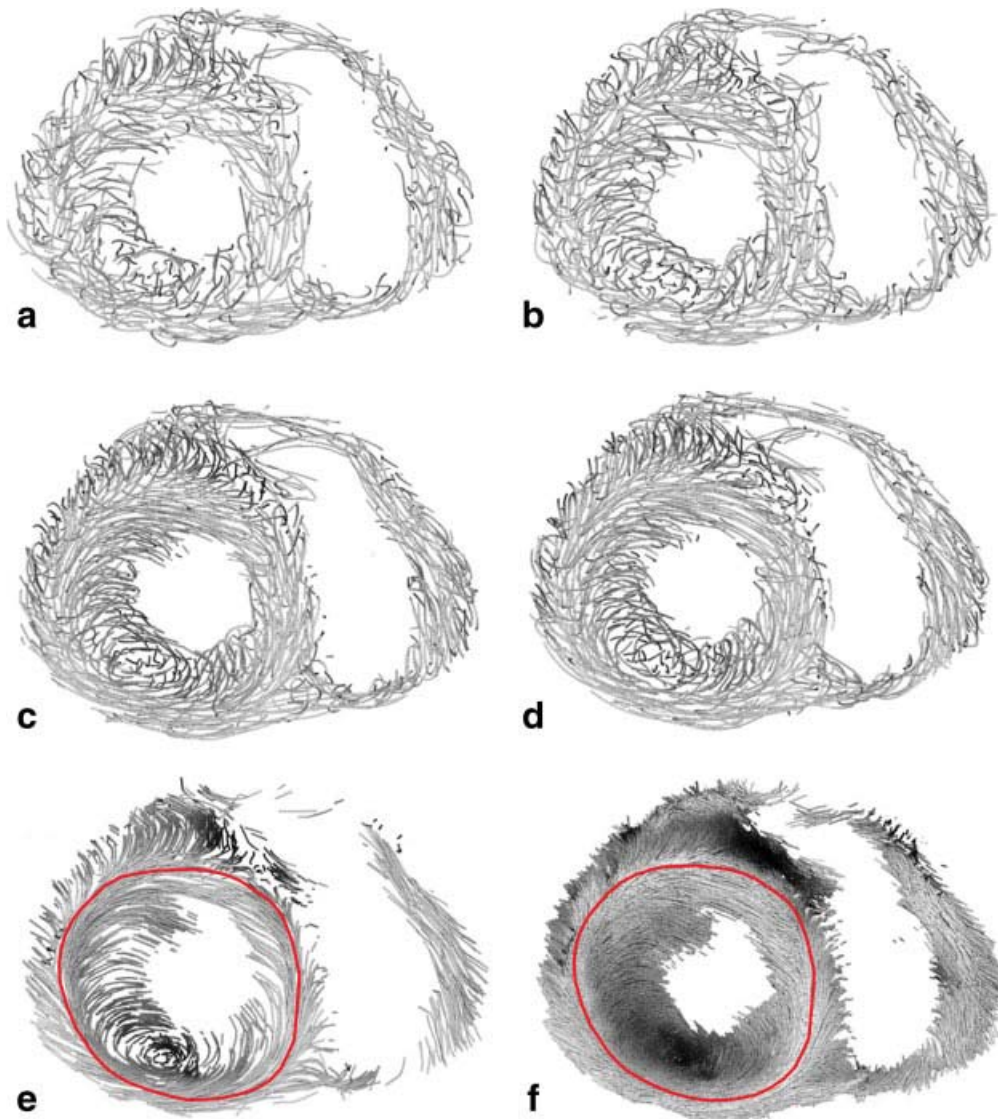
FIG. 17. Fiber tract estimations from a real cardiac dataset: short-axis cut (4 mm thick). The displayed fiber bundles have length greater than 50 mm. (**a**) ICM with $\alpha = 1$ using (t_2)-moves, (**b**) ICM with α-relaxation using (t_2)- and (t_4)-moves, (**c**) SA with communication q_2 and $10^4|E|$ iterations, (**d**) SA with communication q_2 and $10^5|E|$ iterations, (**e**) streamlining with an integration step of 1, and (**f**) streamlining with integration step of 0.1. [Color figure can be viewed in the online issue, which is available at wileyonlinelibrary.com.]

fibers with homogeneous length and density by allowing a more significant local error for the orientation than does streamlining.

Our approach provides more accurate results than streamlining with an integration step of 1 when the PSNR is smaller than 15 dB (this unit integration step approximatively corresponds to the distance between neighboring vertices in our graph structure or, equivalently, between neighboring voxels in the DW volumes) and with an integration step of 0.1 when the PSNR is smaller than 12 dB. In fact, for low PSNR the global nature of our approach overcomes the error summation resulting from the incremental and local nature of streamlining; it is less sensitive to noise.

Yet, the measure $\mathcal{E}(\phi_i)$ is relevant when applied to a population of fibers with significant and homogeneous length. This is the case of our method but not of streamlining, especially when the PSNR is low. Therefore, to better assess the quality of the reconstructed fibers, we propose to weight

$\mathcal{E}(\phi_i)$ by the inverse of the length of the fiber ϕ_i. In other words, we consider the quality indicator:

$$\tilde{\mathcal{E}}(\phi_i) = \frac{\mathcal{E}(\phi_i)}{L(\phi_i)}. \qquad [24]$$

Figure 16 displays the mean value of $\tilde{\mathcal{E}}(\phi_i)$ as a function of the noise level. The arrangement is the same as in Fig. 15. From this viewpoint, our approach provides more accurate results than streamlining with an integration step of 1 when the PSNR is smaller than 26 dB and with an integration step of 0.1 when the PSNR is smaller than 17 dB. Note that the noisy character of the curves in Figs. 16 and 17 associated with standard ICM algorithm can be explained by the deterministic nature of this algorithm. Indeed, the proposed solution can vary significantly depending on the initialization and on the noise realization. This behavior is mainly observed for low PSNR values as the difficulty
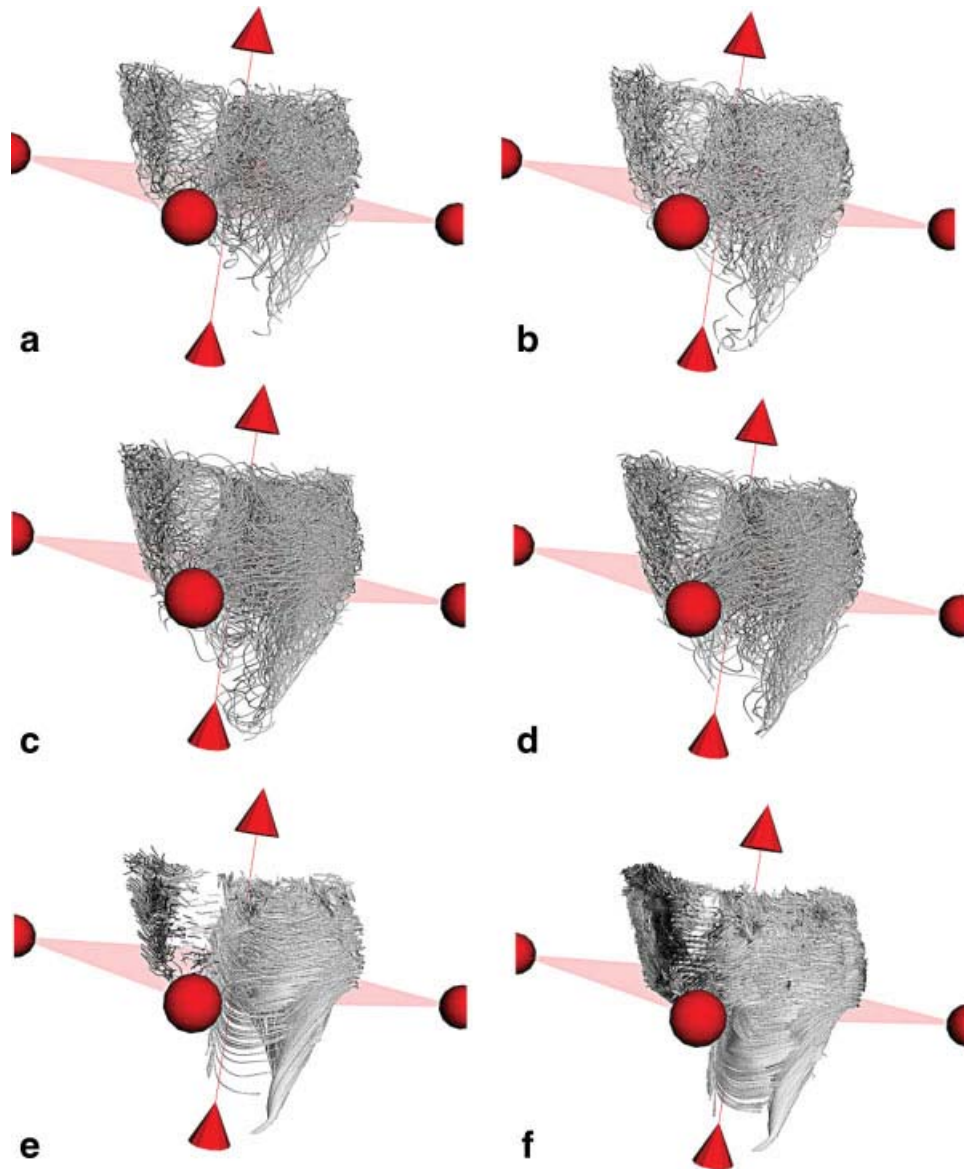
FIG. 18. Fiber tract estimations from a real cardiac dataset: the red plane is the short-axis cut considered in Fig. 18, and the fiber bundles displayed below this plane are the ones going through it. The arrangement is the same as in Fig. 17. [Color figure can be viewed in the online issue, which is available at wileyonlinelibrary.com.]

of the energy landscape increases with noise. The curves associated with our improved ICM algorithm are not noisy because the communication neighborhood is wider, which translates to an energy landscape with fewer local minima.

Similar results are obtained when considering 124-connectivity; however, in this case, the mean fiber error is overall greater than with 26-connectivity, which is a consequence of the fact that 124-connectivity leads to estimated fibers with greater length.

Real Cardiac Data

We applied the tractography approach described in Section "Synthetic Data" to the 16 ex vivo human hearts (PSNR $\approx$ 16 dB). Note that a mask was applied to the DT field to initialize our graph-based approach; the segmentation was performed by selecting the voxels in the reference DW volume whose intensity belongs to the characteristic intensity range of muscles in T2-weighted MR images. Our results are summarized in the following two paragraphs.

Qualitative Analysis

Figures 17 and 18 show the estimation of fiber bundles from the real cardiac dataset using our graph-based approach with 26-connectivity and using the streamlining approach. The streamlining approach was run with integration steps of 0.1 and 1; the criteria for stopping the tracking are thresholds on fractional anisotropy (FA $\leq$ 0.08) and on curvature (the angle between two successive principal directions is kept smaller than 18°). The results associated with the graph-based approach were obtained using (a) ICM with a fixed value of the parameter α in (Eq. [7] [$\alpha = 1$] and

Table 5
Quantitative Results Associated with Estimations from Real Cardiac Data

	Scheme	Method	Comp. time	Fiber count	Mean fiber length	Dispersion	Energy
Graph	t_1	ICM	1	4852	13.71	0.4530	0.5952
approach	q_1	SA $(10^4|E|)$	20	1768	39.84	0.7769	0.3960
		SA $(10^5|E|)$	201	1456	48.77	0.8349	0.3662
	t_2	ICM	2	2204	26.28	0.6994	0.4715
	q_2	SA $(10^4|E|)$	30	1427	49.85	0.8123	0.3738
		SA $(10^5|E|)$	298	1528	55.37	0.8411	0.3399
	t_1	ICM	3	2083	14.05	0.4676	0.5524
	t_2	+	4	2163	29.53	0.7003	0.4336
	$t_2 \bigcup t_4$	relaxation	6	1556	38.36	0.7866	0.3937
Stream.	rk 4	step = 1.0	12	9002	30.12	2.4176	None
approach	rk 4	step = 0.1	96	15,337	35.20	2.4834	None

edge-pair moves, (b) ICM with gradual increase of α and both edge-pair moves and "crossing scheme" moves, and (c,d) SA with edge-pair moves.

When using the proposed graph-based approach with SA, the fiber-bundle prediction seems to be more chaotic. This visual impression can be explained by the fact that our approach predicts several organized fiber-bundle sheets. In fact, we can see from Figs. 17(c,d) that our approach produces peripheral fiber-bundle sheets in addition to the central fiber-bundle sheet obtained with streamlining (i.e., the central sheet displayed in red in Fig. 17f, from which all the other fibers run away), which is in accordance with histological studies (16). Hence, the graph-based approach may provide more reliable information about the human heart architecture than does streamlining.

Quantitative Analysis

Table 5 gives the computation time, the fiber bundle count, the mean fiber length, the fiber-length dispersion, and the energy using streamlining and using the proposed graph-based approach with 26-connectivity. Fibres with length smaller than 4 mm were not taken into account. In the case of streamlining, the number of seeds for the initialization step is equal to the number of voxels, and redundant fiber bundles are removed. Computation times are divided by the computation time corresponding to ICM with $\alpha = 1$ and (t_1)-moves.

The quantitative results obtained from the real cardiac dataset are coherent with those associated with the synthetic datasets. We can see that SA provides lower energies (and hence better approximations to the global fibrous structure according to our model) than classical ICM. The proposed deterministic optimization strategy (ICM with α-relaxation and $(t_2)+(t_4)$-moves) shows similar performance to SA with communication q_1, and the corresponding computational gain is $\frac{20}{6} \sim 3.33$.

The graph-based approach together with either SA or our modified ICM algorithm presents longer fiber bundles and lower fiber-length dispersion. Furthermore, our approach produces a more compact representation of the cardiac fibrous architecture than does streamlining, and our modified ICM algorithm reconstructs the human heart organization faster (the corresponding computational gain is $\frac{12}{6} = 2$).

CONCLUSION

We presented an original way of performing deterministic tractography, which gives an all-paths estimation for the whole DT-MRI volume in one shot and in a completely automatic way. This approach uses local tensor parameters and is guided by a global cost functional that favors the formation of fiber tracts supported by the whole diffusion data. It has low noise sensitivity and produces fiber populations with significant mean length, low length dispersion, and homogeneous density, which makes it particularly well adapted to cardiac imaging. More specifically, our graph-based approach provides more accurate fiber estimations (smaller fiber error) than does streamlining with a unit integration step when the PSNR is smaller than 26 dB and with an integration step of 0.1 when the PSNR is smaller than 17 dB; it also gives more stable mean fiber length, fiber length dispersion, and fiber number as the noise increases.

Our results with real data (PSNR $\approx$ 16 dB) corroborate this findings. Streamlining is more sensitive to noise because of its local nature and because noisy estimations of fractional anisotropy and curvature lead to erroneous terminations of the tractography process. By contrast, our approach yields all the fiber bundles representing a DT-MRI volume with a uniform density (one fiber bundle per voxel).

The proposed deterministic optimization strategy shows performances similar to annealing for both synthetic and real data, but it runs substantially faster than annealing and streamlining. Moreover, our approach does not require seed initialization and does not rely on the choice of hyperparameters. It accurately captures the principal fiber bundles in one shot, and it provides an optimal balance between the density of fiber bundles and the amount of available data. This is particularly interesting for a better understanding of the architecture and organization of the cardiac muscle continuum.

ACKNOWLEDGMENTS

REFERENCES

1. Basser PJ, Pajevic S, Pierpaoli C, Duda J, Aldroubi A. In vivo fiber tractography using DT-MRI data. Magn Reson Med 2000;44: 625–632.

2. Mori S, Crain BJ, Chacko VP, van Zijl PC. Three-dimensional tracking of axonal projections in the brain by magnetic resonance imaging. Ann Neurol 1999;45:265–269.

3. Conturo T, Lori N, Cull T, Akbudak E, Snyder A, Shimony J, McKinstry R, Burton H, Raichle M. Tracking neuronal fiber pathways in the living human brain. Proc Natl Acad Sci USA 1999;96:10 422–10 427.

4. Lu Y, Aldroubi A, Gore JC, Anderson AW, Ding Z. Improved fiber tractography with bayesian tensor regularization. NeuroImage 2006; 31:1061–1074.

5. Behrens T, Woolrich M, Jenkinson M, Johansen-Berg H, Nunes R, Clare S, Matthews P, Brady J, Smith S. Characterization and propagation of uncertainty in diffusion-weighted MR imaging. Magn Reson Med 2003;50:1077–1088.

6. Parker GJ, Haroon HA, Wheeler-Kingshott CA. A framework for a streamline-based probabilistic index of connectivity (PICo) using a structural interpretation of MRI diffusion measurements. J Magn Reson Imaging 2003; 18:242–254.

7. Friman O, Farnebäck G, Westin C. A bayesian approach for stochastic white matter tractography. IEEE Trans Med Imaging 2006;25: 965–978.

8. Parker GJ, Wheeler-Kingshott CA, Barker GJ. Estimating distributed anatomical brain connectivity using fast marching methods and diffusion tensor imaging. IEEE Trans Med Imaging 2002;21:505–512.

9. O'Donnell L, Haker S, Westin CF. New approaches to estimation of white matter connectivity in diffusion tensor mri: elliptic pdes and geodesics in a tensor-warped space. Proc. Int. Conf. Medical Image Computing, Computer Assisted Intervention, Tokyo, Japan, 2002. pp 459–466.

10. Lenglet C, Deriche R, Faugeras O. Inferring white matter geometry from diffusion tensor MRI: application to connectivity mapping. Proc. Eur. Conf. Computer Vision, Prague, Czech Republic, 2004.

11. Jackowski M, Kaod CY, Qiua M, Constablea RT, Staiba LH. White matter tractography by anisotropic wavefront evolution and diffusion tensor imaging. Med Image Anal 2005;9:427–440.

12. Iturria-Medina Y, Canales-Rodrguez EJ, Melie-Garca L, Valds-Hernndez PA, Martnez-Montes E, Alemn-Gmez Y, Snchez-Bornotb JM. Characterizing brain anatomical connections using diffusion weighted mri and graph theory. NeuroImage 2007;36:645–660.

13. Zalesky A. DT-MRI fiber tracking: a shortest paths approach. IEEE Trans Med Imaging 2008;27:1458–1471.

14. Mangin JF, Poupon C, Cointepas Y, Riviere D, Papadopoulos-Orfanos D, Clark CA, Rgis J, Bihan DL. A framework based on spin glass models for the inference of anatomical connectivity from diffusion-weighted mr data. NMR Biomed 2002;15:481–492.

15. Fillard P, Poupon C, Mangin JF. A novel global tractography algorithm based on adaptative spin glass model. Proc. Int. Conf. Medical Image Computing, Computer Assisted Intervention, London, UK, 2009. pp 927–934.

16. Anderson RH, Ho SY, Sanchez-Quintana D, Redmann K, Lunkenheimer PP. Heuristic problems in defining the three-dimensional arrangement of the ventricular myocytes. Anat Rec 2006;288:579–586.

17. Scollan DF, Holmes A, Winslow RL, Forder J. Histological validation of myocardial microstructure obtained from diffusion tensor magnetic resonance imaging. Am J Physiol Heart Circ Physiol 1998;275:H2308–H2318.

18. Tseng WYI, Dou J, Reese TG, Wedeen VJ. Imaging myocardial fiber disarray and intramural strain hypokinesis in hypertrophic cardiomyopathy with mri. J Magn Reson Imaging 2006;23:1–8.

19. Firtenberg MS, Thomas JD. Benign cardiac tumors. E-medicine from WebMD 2007. Available at http://www.emedicine.com/med/topic2999.htm. Accessed July 6, 2010.

20. Winkler G. Image analysis, random fields and Markov chain Monte carlo methods, 2 ed., Berlin: Springer Verlag; 2003.

21. Kirkpatrick S, Gelatt CD, Vecchi MP. Optimization by simulated annealing. Science 1983;220:671–680.

22. Besag J. On the statistical analysis of dirty pictures. J R Stat Soc Ser B 1986; 48:259–302.

23. Geman S, Geman D. Stochastic relaxation, Gibbs distributions, and the Bayesian restoration of images. IEEE Trans Pattern Anal Mach Intell 1984;6:721–741.

24. Hajek B. Cooling schedules for optimal annealing. Math Oper Res 1988;13:311–329.

25. Chiang TS, Chow Y. On the convergence rate of annealing processes. SIAM J Control Optim 1988;26:1455–1470.

26. Catoni O. Rough large deviation estimates for simulated annealing: application to exponential schedules. Ann Probab 1992;20:1109–1146.

27. Robini MC, Rastello T, Magnin IE. Simulated annealing, acceleration techniques and image restoration. IEEE Trans Imag Proc 1999;8:1374–1387.

28. Frindel C, Robini M, Rapacchi S, Stephant E, Zhu YM, Croisille P. Towards in vivo diffusion tensor MRI on human heart using edge-preserving regularization. Proc. 29th Int. Conf. IEEE EMBS, Lyon, France, 2007. pp 6007–6010.